Biomechanics and Modeling in Mechanobiology
https://doi.org/10.1007/s10237-023-01783-6

ORIGINAL PAPER

Physical biology of cell–substrate interactions under cyclic stretch

Siddhartha Jaddivada[1] · **Namrata Gundiah**[1]

Received: 28 June 2023 / Accepted: 14 October 2023

Abstract
Mechanosensitive focal adhesion (FA) complexes mediate dynamic interactions between cells and substrates and regulate cellular function. Integrins in FA complexes link substrate ligands to stress fibers (SFs) and aid load transfer and traction generation. We developed a one-dimensional, multi-scale, stochastic finite element model of a fibroblast on a substrate that includes calcium signaling, SF remodeling, and FA dynamics. We linked stochastic dynamics, describing the formation and clustering of integrins to substrate ligands via motor-clutches, to a continuum level SF contractility model at various locations along the cell length. We quantified changes in cellular responses with substrate stiffness, ligand density, and cyclic stretch. Results show that tractions and integrin recruitments varied along the cell length; tractions were maximum at lamellar regions and reduced to zero at the cell center. Optimal substrate stiffness, based on maximum tractions exerted by the cell, shifted toward stiffer substrates at high ligand densities. Mean tractions varied biphasically with substrate stiffness and peaked at the optimal substrate stiffness. Cytosolic calcium increased monotonically with substrate stiffness and accumulated near lamellipodial regions. Cyclic stretch increased the cytosolic calcium, integrin concentrations, and tractions at lamellipodial and intermediate regions on compliant substrates. The optimal substrate stiffness under stretch shifted toward compliant substrates for a given ligand density. Stretch also caused cell deadhesions beyond a critical substrate stiffness. FA's destabilized on stiff substrates under cyclic stretch. An increase in substrate stiffness and cyclic stretch resulted in higher fibroblast contractility. These results show that chemomechanical coupling is essential in mechanosensing responses underlying cell–substrate interactions.

Keywords Morot clutch · Calcium signaling · Stress fiber · Substrate stiffness

1 Introduction

Cyclically loaded cells, such as arterial fibroblasts, endothelial cells, and smooth muscle cells, must constantly adapt to dynamically changing mechanical loads. Cell remodeling under stretch is vital to the activation of complex biochemical signaling pathways that orchestrate cellular functions related to contractility, differentiation, growth, and migration over a short duration (Ben-Ze'ev et al. 1980; Watt et al. 1988; Wozniak et al. 2004). Mechanotransduction over a longer duration regulates gene expression and protein synthesis that may, over time, cause changes to the underlying extracellular matrix (ECM) properties and contribute to the progression of diseases such as fibrosis and aneurysm growth (Janmey et al. 2009; Humphrey and Rajagopal 2002).

Heterodimeric transmembrane proteins, integrins, are an important component of focal adhesion (FA) complexes and mediate the complex interactions between cells and substrates (Janmey et al. 2009). Integrins attach to the ECM through their extracellular domains, connect to cytoskeletal stress fibers (SFs) via intracellular domains, and permit bidirectional signaling between the cell and the substrate (Hynes 2002). Several distinct, multi-protein assemblies in the FA complexes contribute to the downstream cell signaling cascades (Winograd-Katz et al. 2014; Livne and Geiger 2016; Byron et al. 2011). Scaffolding and adaptor FA proteins, such as vinculin, paxillin, talin, and zyxin, link the SF to the ECM via integrins, whereas signaling proteins are locally recruited to generate and mediate the development and maturation of FA under mechanical stimuli (Winograd-Katz et al. 2014; Gallant et al. 2005; Paddillaya et al. 2022).

✉ Namrata Gundiah
namrata@iisc.ac.in; ngundiah@gmail.com

[1] Department of Mechanical Engineering, Indian Institute of Science, Bangalore 560012, India

Published online: 27 November 2023

Integrins cluster and corral into adhesomes (Takagi et al. 2002) in the presence of extracellular magnesium from the ECM (Tiwari et al. 2011) and cytoplasmic forces (Kechagia et al. 2019). Forces cause conformational changes in the integrin structure that alter them from a *bent* to an *extended* state and initiate downstream signaling when coupled to the SFs (Balaban et al. 2001). Reinforcement and maturation of integrins link them to proteins, such as talin, tensin, α-actinin, and vinculin, collectively called *adaptor proteins*, which increase the size, shape, and molecular composition of the adhesome (Kumar et al. 2016; Galbraith et al. 2002). These change in response to forces applied by the SF or through cyclic substrate stretch (Swaminathan et al. 2017). Fibroblasts under uniaxial cyclic stretch reorient orthogonal to the stretch direction at high frequencies (> 1 Hz) and amplitudes over 5% and alter the integrin density (Chagnon-Lessard et al. 2017; Wang et al. 2004; Livne et al. 2014; De 2018). Tendon fibroblasts express higher levels of α-smooth muscle actin and phospholipase A2 when oriented parallel to the stretching direction (Wang et al. 2004). Endlich and coworkers showed that actin polymerization and force in SF caused centripetal movement of actin at 0.2–0.4 μm/min in SF attached to FAs. Both substrate deformations and FA de-adhesions permit the sliding of FAs and caused SF deformations and actin flows in cells (Endlich et al. 2007). Growth and remodeling of SFs are hypothesized to be essential to the re-orientational responses of cells under cyclic stretch (Chatterjee et al. 2022).

Chan and Odde modeled the physical coupling of cells on elastic substrates using spring-like molecular clutches, representing adaptor proteins, that generate tractions and stochastically form or break (Chan and Odde 2008; Elosegui-Artola et al. 2014; Bangasser et al. 2013). Individual clutches reversibly engage to the substrate resulting in tension build-up in successfully engaged clutches that link to the cytoskeletal actin. Myosin motors cause a retrograde flow of actin and work against the resistance provided by the engaged clutches. This results in two modes of interaction: a stalled mode that generates high tractions and adhesions, and a load-and-fail mode with lower tractions and adhesions (Bangasser et al. 2013). The model demonstrated an optimum substrate stiffness based on the maximum tractions exerted by cells on substrates. The model did not however incorporate chemical signaling, associated with integrins, and the corresponding changes in SF activation caused by clutch engagements.

Cell tractions on substrates show an initial monotonic increase with increasing substrate stiffness and higher ligand affinity; FA sizes also increased linearly with force (Balaban et al. 2001; Muller and Pompe 2016). Deshpande and colleagues developed a generalized model to represent the SF cross-bridge dynamics and quantified the cellular response to varied substrate compliance (Deshpande et al. 2006). Strong spatial gradients in SF contractility are present along the cell length through coupled Rho signaling at integrin attachment sites (Besser and Schwarz 2007). Cyclic stretching of dermal fibroblasts causes upregulation in F-actin expression and myosin (Huang et al. 2013). The corresponding increased tractions under cyclic stretch is accompanied with higher cell stiffness (Chatterjee et al. 2022) and intracellular calcium transients via stretch-activated channels (Arora et al. 1994; Murata et al. 2014). Increased calcium flux under stretch also depends on the activation of phosphatidyl-inositol pathway, induced by membrane perturbations, which suggests a possible role for FA clustering (Arora et al. 1994).

How do dynamic changes in integrin recruitments, coupled to SF contractility, result in the development of tractions in cyclically stretched cells? We develop a novel 1D multi-scale model of a fibroblast to include biochemical signaling and remodeling of the cytoskeleton and FA dynamics at different locations along the cell length. We quantify changes to the SF contractility, FA remodeling, and chemical signaling in response to external cyclic mechanical stretch. We also test how cellular responses are altered with substrate stiffness and ligand density that are relevant in the context of tissue fibrosis. Our results show the importance of calcium dynamics in delineating differences in the cell tractions under cyclic stretch. Chemomechanical coupling of the SF and FA dynamics is also useful to characterize the individual roles of adaptor proteins, such as talin, in mechanosensing.

2 Methods

2.1 A computational model of cell contractility and adhesion formation

We used a systems biology approach to model cell-substrate interactions under cyclic stretch. Deformations during cell-substrate interactions were calculated using a one-dimensional stochastic finite element method (SFEM). The substrate and SF were discretized into 14 and 28 elements respectively (Fig. 1a) to explore spatial differences in FA and tractions under static and stretch conditions. The cell includes a lamellipodia region, located between nodes 1–3 and 27–29, and lamellar regions, located at nodes 3–9 and 21–27, on either side of the cell center. Ligands with a uniform concentration on the substrate attach to integrins in the cell membrane and connect the other structural adaptor proteins (clutches) to the contractile SF (Fig. 1b, c). The model consists of different modules that couple mechanics at hierarchical scales ranging from the stochastic dynamics of individual clutches to the continuum level SF contractility that includes calcium signaling.

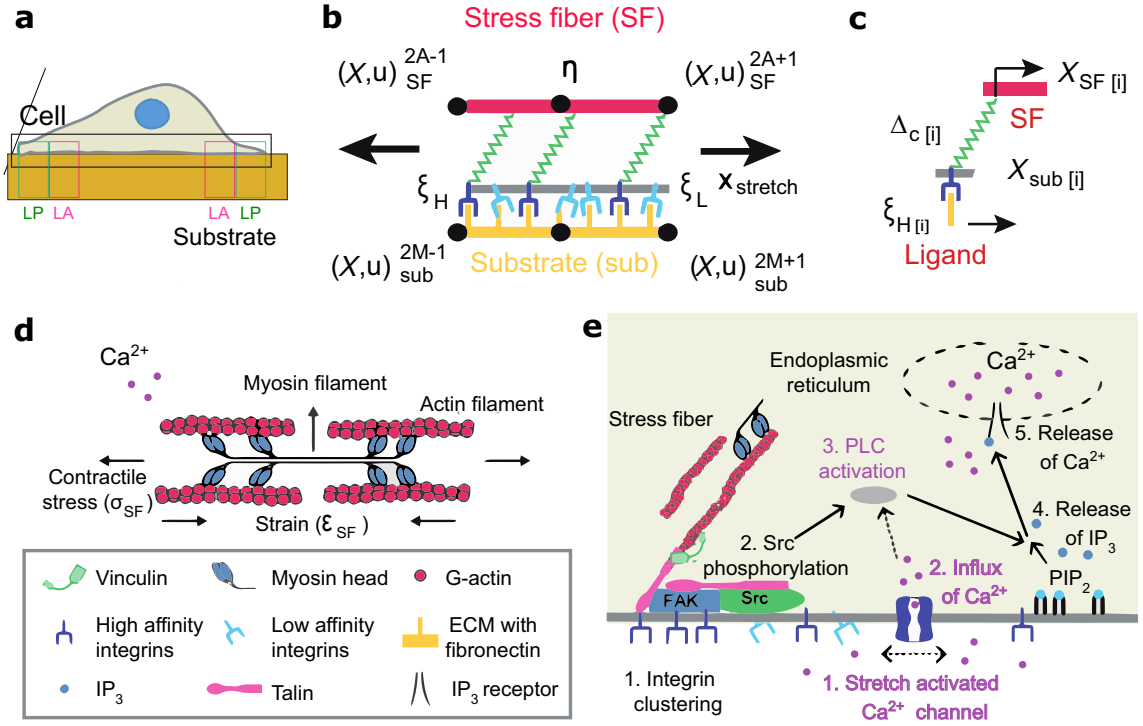

Fig. 1 **a** Schematic representation of the cell attached to the substrate (sub). The box region is the domain is considered in this work. Lamellipodial (LP) and lamellar (LA) regions of the cell are also indicated. **b** An assembly of representative FE elements used to model cell–substrate interactions. The FE element spans stress fiber (SF) nodes 2A−1 and 2A+1 and substrate nodes 2M−1 and 2M+1. The cell membrane (gray) with integrins attaches to a ligand coated substrate (yellow). $(x,\mathrm{u})^{\mathrm{A}}_{\mathrm{SF}}$ and $(x,\mathrm{u})^{\mathrm{M}}_{\mathrm{sub}}$ are nodal positions and displacements for the SF and substrate, respectively. **c** Adaptor proteins (green) attach the *i*th ligand on the substrate through high-affinity integrin attachments to the SF's (red) with activation, η^{A}. Deformations, $\Delta_{c[i]}$, between the clutch attachment points at SF $x_{\mathrm{SF}[i]}$, and the substrate, $x_{\mathrm{sub}[i]}$, results in changes to the concentrations of high-affinity, ξ_{H}, and low-affinity integrins, ξ_{L}, at the cell membrane. The concentration of high affinity integrins at the bottom end of the clutch is represented as $\xi_{\mathrm{H}[i]}$. **d** Interactions between actin and myosin filaments through cross-bridge cycling induce contractile stress ($\boldsymbol{\sigma}_{\mathbf{SF}}$) and strain ($\boldsymbol{\varepsilon}_{\mathbf{SF}}$) in the presence of calcium. **e** Calcium signaling in the model has two possible pathways that include integrin clustering (black) or result due to membrane stretch (purple). Both pathways result in PLC activation in the cell

The stochastic module includes the engagement/disengagement of clutches between the SF and the substrate characterized with Young's modulus, E_{sub}, and containing a uniform fibronectin coating with defined ligand densities, n_{c} (Chan and Odde 2008; Elosegui-Artola et al. 2014; Bangasser et al. 2013; Muller and Pompe 2016). Cell–substrate interactions are delineated into four different phases: (i) formation of reversible bonds between high-affinity integrins and ligands, (ii) clustering of high-affinity integrins at FA complexes, (iii) recruitment of structural adaptor proteins by integrin clusters in the FA, and (iv) contractility due to SF attachment to adaptor proteins (Ward and Hammer 1993; Lotz et al. 1989). SF contractility due to cross-bridge cycling between actin and myosin requires calcium (Fig. 1d) and results in deformations of adaptor proteins and the ligand coated substrate. Both integrin dynamics at FAs and stretch-dependent ion channels are associated with calcium flux in the cell (Fig. 1e) that is described using a signaling module (Arora et al. 1994; Nishitani et al. 2011). Calcium feedback is especially important in the context of cells under cyclic stretch (Arora et al. 1994; Murata et al. 2014).

3 Motor-clutch stochastic dynamics

We use the motor-clutch model to simulate interactions between the SF and ligands attached uniformly to a linearly elastic ECM substrate (Fig. 1a). Ligands in each element

are in a disengaged state at the start of the simulation; these engage/ disengage stochastically through clutches (Bangasser et al. 2013). Figure 1a shows a representative SF element with clutches that reversibly bind with rate,$k_{\mathrm{on}[i]}$, to the SF and the ith ligand on the substrate and disengage with a force-dependent rate, $k_{\mathrm{off}[i]}$, given by the Bell model for slip bonds (Bell 1978) as

$$k_{\mathrm{off}[i]} = k^0_{\mathrm{off}} * \exp\left(\frac{F_{c[i]}}{F_{\mathrm{b}}}\right) \tag{1}$$

k^0_{off} is the unloaded clutch off-rate, F_b is the characteristic rupture force, and $F_{c[i]}$ is the force transmitted by the clutch to the substrate in element A located on the SF, given by

$$F_{c[i]} = k_c * \Delta_{c[i]} \tag{2}$$

where k_{c} is the stiffness of the clutch in this expression.

Clutches resist the actin retrograde flow caused by active stress, σ_{SF}, generated in the SF. Engaged clutches are subject to deformations, $\Delta_{\mathrm{c}[i]}$, due to the active SF stress. The dynamics of clutch engagements/ disengagements were obtained using Monte Carlo simulations. In this method, the ensemble of clutches at each element of the cell was initially assigned uniform random numbers ($0 \leq URN_{[i]} \leq 1$). The off-rate for each engaged clutch was determined using $F_{c[i]}$ in Eq. 1. The event times for engagement, $t_{\mathrm{on}[i]}$, or disengagement, $t_{\mathrm{off}[i]}$, of the ligand, i, in element A were calculated using the equation below.

$$t_{\mathrm{on}[i]} = -\frac{\ln\left(URN_{[i]}\right)}{k_{\mathrm{on}[i]}} \text{ and } t_{\mathrm{off}[i]} = -\frac{\ln(URN_{[i]})}{k_{\mathrm{off}[i]}} \tag{3}$$

The position $x_{\mathrm{SF}[i]}$ of n^A_{eng} engaged clutches in the SF element from the previous iteration was updated (Chan and Odde 2008) over the minimum event time $\left(t_{\mathrm{on/off}} = \min\left(\frac{t_{\mathrm{on}[i]}}{t_{\mathrm{off}\ [i]}}\right)\right)$.

$$x_{\mathrm{SF}[i]} = x_{\mathrm{SF}[i]} + v_{\mathrm{SF}[i]} * t_{\mathrm{on/off}} \tag{4}$$

$v_{\mathrm{SF}[i]}$ is the rate of deformation of the SF at the clutch attachment point, which was calculated using the FEM. The clutch deformation, $\Delta_{\mathrm{c}[i]}$, was determined using the difference in coordinates of the clutch attachment points on the SF, $x_{\mathrm{SF}[i]}$, and the substrate, $x_{\mathrm{sub}[i]}$. Clutch deformation is also equivalent to the difference in the displacements of attachments at SF, $u_{\mathrm{SF}[i]}$, and the substrate , $u_{\mathrm{sub}[i]}$

$$\Delta_{c[i]} = x_{\mathrm{SF}[i]} - x_{\mathrm{sub}[i]} = u_{\mathrm{SF}[i]} - u_{\mathrm{sub}[i]} \tag{5}$$

The transmitted force, $F_{c[i]}$, and cyclic stretch, x_{stretch}, results in a local substrate displacement, $x^{\mathrm{M}}_{\mathrm{sub}}$. The corresponding change in the position of ligand attachments between nodes 2M−1 and 2M+1 of the substrate, $x_{\mathrm{sub}[i]}$, was determined using interpolation. Mechanical stiffness of the clutches, k_c, and the substrate, E_{sub}, determines the resistance to clutch loading by the SF.

4 Contractility module

We used a continuum-level contractility module to quantify the SF activation kinetics characterized through coupling of the calcium-dependent cross-bridge cycling (Fig. 1d), and the tension-dependent SF assembly/ disassembly. We use a first-order rate equation to parametrize the assembly/disassembly of SF bundles using a non-dimensional activation parameter, η, at each location in the cell which is given by (Bell 1978)

$$\dot{\eta} = \left[(1-\eta)\right]\frac{C\overline{\mathrm{K}}_{\mathrm{f}}}{t^c} - \left[\left(1 - \frac{\sigma_{\mathrm{SF}}}{\sigma_0}\right)\right]\eta\frac{\overline{\mathrm{K}}_{\mathrm{b}}}{t^c} \tag{6}$$

η is the ratio of the concentration of polymerized actin and phosphorylated myosin in the SF to their maximum possible concentrations. $\overline{K}_f$, $\overline{K}_b$ are rate constants that govern the formation and dissociation of SF's with a time constant, t^c. C is the concentration of calcium, σ_{SF} is the stress in the SF, and σ_0 is the isometric stress of the SF. Equation 6 shows that the rate of SF assembly decreases with SF activation at each element, A, and is proportional to calcium availability. In contrast, SF dissociation is directly proportional to the activation at each node and is a function of the SF stress. The dissociation rate is zero when the fibers are held at their isometric stress, σ_0, at each element and increases linearly at lower stress.

The choice of isometric stress value is an important aspect of the simulation. The SF becomes stable at isometric stress, σ_0, as the term involving the dissociation rate constant, $\overline{\mathrm{K}}_{\mathrm{b}}$, becomes zero from Eq. 6 (Deshpande et al. 2006). Experiments suggest that the SFs stabilize at an isometric stress when anchored to gels and lack SF in free-floating collagen gels (Burridge and Chrzanowska-Wodnicka 1996). Fibroblasts have prominent stress fibers on substrates that cause gel contraction; SFs undergo dissociation upon cell release from the substrate (Mochitate et al. 1991; Grinnell 1994). Alternative methods may be employed to incorporate SF kinetics within the model. For example, SF can assume to be fully active ($\eta = 1$) throughout simulation (De 2018). Elson and Genin modeled the SF to be stable at a predefined homeostatic stretch value in lieu of σ_0 (Elson and Genin 2013). A change in the SF activation kinetics will influence the reported forces and their sensitivity to external stimuli like substrate stiffness. We assume that the isometric stress of the SF at each element, σ_0, is directly proportional to the activation level of the SF, $\sigma_0 = \eta\sigma_{\mathrm{max}}$ where σ_{max} is the isometric stress during the maximum possible concentration of the polymerized actin and phosphorylated myosin in the SF. The value of σ_{max} was assumed to be a product of the myosin motor concentration, n_{m}, and maximum force generated by

individual motors, F_m. $\sigma_{\max}$ in each element is generated by cross-bridge cycling similar to that in muscle cells (Fig. 1d). We used a Hill-like relation to model the tension in the SF based on the rate of extension/shortening given by

$$\frac{\sigma_{\mathrm{SF}}}{\sigma_0} = \begin{cases} 0, & \frac{\dot{\varepsilon}_{SF}}{\dot{\varepsilon}_0} < 0 \\ 1 + \frac{\overline{K}_v}{\eta}\left(\frac{\dot{\varepsilon}_{SF}}{\dot{\varepsilon}_0}\right), & -\frac{\eta}{\overline{K}_v} \le \frac{\dot{\varepsilon}_{SF}}{\dot{\varepsilon}_0} \le 0 \\ 1, & \& \frac{\dot{\varepsilon}_{SF}}{\dot{\varepsilon}_0} > 0 \end{cases}. \tag{7}$$

$\dot{\varepsilon}_{\mathrm{SF}}$ is the rate of change in the SF length, which is positive for lengthening and negative for shortening. The non-dimensional constant, $\overline{K}_v$, is the fractional reduction in stress when the shortening rate increases by the isometric value, $\dot{\varepsilon}_0$.

5 Biochemical coupling of calcium signaling

Cyclic stretching of the membrane causes a release of calcium ions that alters the SF contractility (Nishitani et al. 2011). Calcium flux is modeled using two signaling pathways: first, through changes in the concentration of high-affinity integrins, ξ_H, at the base of engaged clutches. Second, membrane stretch, u_{memb}, which causes activation of stretch-activated calcium ion channels that result in downstream signaling (Fig. 1e). Membrane stretch was assumed to be proportional to the displacement, u_{sub}, in the substrate.

We calculated the density of high-affinity integrins, $\xi_{H[i]}$, at every ligand i in SF element A, as a ratio of the reference concentration of integrins, ξ_R, to the change in chemical energy due to integrin conformation change in the presence of variable clutch force (Bell 1978).

$$\xi_{H[i]} = \frac{\xi_{\mathrm{R}}}{\left(\exp\left[\frac{\mu_{\mathrm{H}} - \mu_{\mathrm{L}} + \psi_{c[i]} - F_{c[i]}\Delta_{c[i]}}{\mathrm{k}\theta}\right]\right) + 1} \tag{8}$$

The denominator includes terms for the difference in chemical potentials between high- and low-affinity integrins, $(\mu_{\mathrm{H}} - \mu_{\mathrm{L}})$, stretch energy in the integrin—ligand complex for each ligand ($\psi_{c[i]}$, and the work conjugate ($F_{c[i]}\Delta_{c[i]}$) term. Equation 8 hence accounts for integrin clustering that is altered due to variable clutch force induced by the SFs and substrate stretch.

High-affinity integrins initiate the production of a signaling molecule, IP_3, that diffuses and gets de-phosphorylated within the cytosol. IP_3 induce the opening of calcium gated channels in the endoplasmic reticulum (ER). The rate change in the concentration of IP_3, S, at a specific location, x_i, was determined using a reaction–diffusion equation by (Bell 1978)

$$\dot{S} = m_s k\theta \frac{\partial^2 S}{\partial x_i^2} - \kappa_d S + S\dot{\varepsilon} \tag{9}$$

m_s represents the motility of IP_3 in the cell, k is the Boltzmann's constant, and θ is the absolute temperature. The rate equation also includes the de-phosphorylation of IP_3 described with a reaction rate, k_d. The last term in the equation accounts for the effects of cell stretch on calcium dynamics via the strain rate, $\dot{\varepsilon}$. The flux boundary condition over the cell boundary with outward normal, n_i, is given by

$$m_s \kappa\theta\left(n_i \frac{\partial S}{\partial x_i}\right) = -\alpha \max(0, \dot{\xi}_{\mathrm{H}}) \tag{10}$$

An increase in ξ_{H} with time hence results in the production of IP_3 with a non-dimensional proportionality constant α (Bell 1978).

The concentration of calcium ions in the cytosol was normalized with respect to the maximum calcium in cells to C ($0 \le C \le 1$). The rate equation for C is obtained assuming first-order kinetics and is given by

$$\frac{\partial C}{\partial t} = \lambda_f \frac{S}{S_0}(1 - c) - \lambda_b c \tag{11}$$

where λ_f is the rate constant governing the rate of release of calcium ions from the IP_3-gated reserve in the endoplasmic reticulum and S_0 is reference IP_3concentration. Calcium increases with S, and its reabsorption into the ER is governed by another rate constant, λ_b, and the calcium concentration, C. These equations are useful to model the role of integrin populations and membrane stretch on the overall calcium at each point in the cell.

6 Coupling between the chemomechanical modules to simulate cell–substrate interactions during static and stretch conditions

We use MATLAB (v8.2 2013a; The Math Works, Natick, MA) to simulate cell-substrate interactions through the SFEM model. The simulation involves temporal integration of three coupled modules through a staggered approach, and a subsequent implementation of mechanical equilibrium in the SF, clutches, and the substrate at the end of each time step. The modules embody stochastic clutch dynamics, calcium signaling, and SF contractility during cell–substrate interaction. Feedback between the different modules involving current and earlier iteration values is indicated in Fig. 2. Mechanical equilibrium of the cell–substrate system was implemented through the following set of coupled equations

$$\frac{\partial \sigma_{\mathrm{SF}}}{\partial x_{\mathrm{SF}}} + F_c^{\mathrm{SF}} = 0 \text{ and} \tag{12}$$

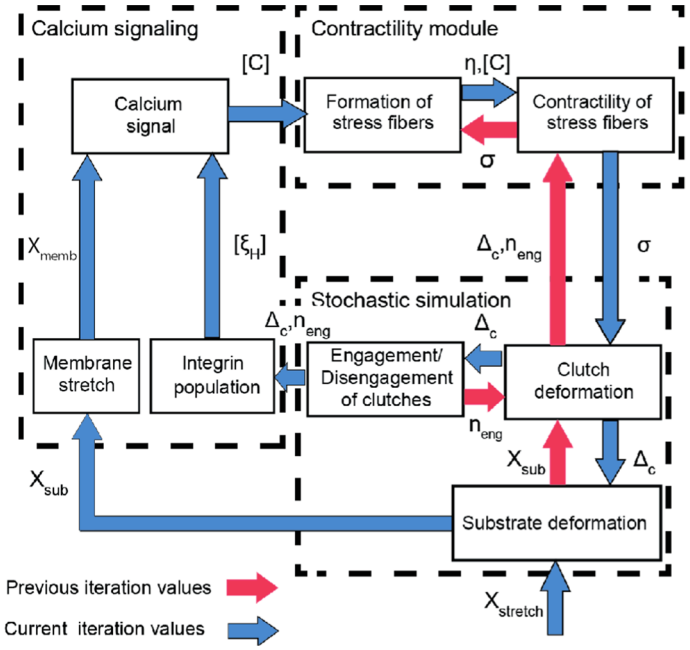

Fig. 2 The cell–substrate interaction model includes stochastic simulations, SF contractility, and calcium signaling modules. Interactions between the different modules are indicated by arrows for the previous and current iteration along with the corresponding variables. Clutches in the cell membrane reversibly engage (n_{eng}) or disengage with the substrate and are modeled through the stochastic module. SF activation (η) in the presence of calcium results in stress (σ_{SF}) that causes deformation (Δ_c) of the engaged clutches, and a corresponding substrate displacement (u_{sub}) that is simulated using the contractility module. u_{sub} and Δ_c causes activation of calcium signal through membrane stretch and aggregation of high-affinity integrins (ξ_H) obtained using the calcium signaling module. The change in calcium (C) is an input in the contractility module

x_{SF} and x_{sub} are the coordinates along the length of cell and substrate domains with unit cross-sectional area, respectively. σ_{SF} is the stress in SF specified by constitutive Eqs. 6 and 7, and σ_{sub} is the stress in the hyperelastic substrate given by

$$\sigma_{sub} = E_{sub}\frac{\partial u_{sub}}{\partial x_{sub}} \tag{13}$$

F_c^{SF} and F_c^{sub} are the forces transferred by clutches to SF and substrate, and respectively, these forces are the summation of clutch forces $F_{c[i]}$ calculated using Eqs. 2 and 5.

$$F_c^{SF} = \sum_{i=1}^{n_{eng}^A} F_{c[i]}\delta^*\left(x_{SF} - x_{SF[i]}\right) \text{and} F_c^{sub} = \sum_{i=1}^{n_{eng}^M} F_{c[i]}\delta^*\left(x_{sub} - x_{sub[i]}\right) \tag{14}$$

In Eq. 14, the Dirac delta function, $\delta^*(x_{SF/sub} - x_{SF/sub[i]})$, ensures that force contribution by clutches, $F_{c[i]}$, is nonzero only at their attachment points $x_{SF[i]}$ and $x_{sub[i]}$. n_{eng}^A and n_{eng}^M are the number of clutches engaged to SF and substrate, respectively, at a given location. Deformations in the cell and substrate are obtained by establishing a weak form of Eq. 12 using the Galerkin procedure. Boundary conditions for SF are given by $\sigma_{SF} = 0$ and $u_{SF} = 0$ at $x_{SF} = \pm L_c$ and $x_{SF} = 0$, respectively. The boundary condition for substrate is given by $u_{sub} = 0$ at $x_{sub} = 0$ and $u_{sub} = 0$ at $x_{sub} = \pm L_s/2$, and for substrate under stretch $u_{sub} = \pm(0.1 \times L_s/4) \times (1 + \sin(2\pi t - \pi/2))$. The variational form of Eq. 12 is given as

$$\begin{aligned}&\int_{-L_c/2}^{L_c/2} \sigma_{SF}\frac{\partial \delta u_{SF}}{\partial x_{SF}}dL - \sum_{i=1}^{n_{eng}} F_{c[i]}^{SF}\delta u_{SF[i]} \\ &= 0 \text{ and } \int_{-L_s/2}^{L_s/2} \sigma_{sub}\frac{\partial \delta u_{sub}}{\partial x_{sub}}dL + \sum_{i=1}^{n_{eng}} F_{c[i]}^{sub}\delta u_{sub[i]} = 0\end{aligned} \tag{15}$$

n_{eng} is the total number of clutches engaged. The linearized form of Eq. 15 at time $t + \Delta t$ is given by

$$\begin{aligned}&\int_{-L_c/2}^{L_c/2} \frac{\partial \delta u_{SF}}{\partial x_{SF}}\frac{\partial \sigma_{SF}}{\partial \epsilon_{SF}}\frac{\partial \Delta u_{SF}}{\partial x_{SF}}dL + \sum_{i=1}^{n_{eng}} k_c(\Delta u_{SF[i]} - \Delta u_{sub[i]})\delta u_{SF[i]} \\ &= -\left(\int_{-L_c/2}^{L_c/2} \sigma_{SF}\frac{\partial \delta u_{SF}}{\partial x_{SF}}dL - \sum_{i=1}^{n_{eng}} F_{c[i]}^{SF}\delta u_{SF[i]}\right)_{t+\Delta t}^{i-1} \text{ and} \\ &\int_{-L_s/2}^{L_s/2} \frac{\partial \delta u_{sub}}{\partial x_{sub}}\frac{\partial \sigma_{sub}}{\partial \epsilon_{sub}}\frac{\partial \Delta u_{sub}}{\partial x_{sub}}dL + \sum_{i=1}^{n_{eng}} k_c(\Delta u_{sub[i]} - \Delta u_{SF[i]})\delta u_{sub[i]} \\ &= -\left(\int_{-L_s/2}^{L_s/2} \sigma_{sub}\frac{\partial \delta u_{sub}}{\partial x_{sub}}dL + \sum_{i=1}^{n_{eng}} F_{c[i]}^{sub}\delta u_{sub[i]}\right)_{t+\Delta t}^{i-1}\end{aligned} \tag{16}$$

The variational equations in Eq. 16 were discretized through 1D quadratic shape functions, H_{SF} and H_{sub}, on cell and substrate domains, respectively. The displacements of domains were interpolated as $u_{\text{sub}\backslash\text{SF}} = \sum_{i=1}^{3} H_{\text{sub}\backslash\text{SF}_i} u_{\text{sub}\backslash\text{SF}}^{2A\pm i}$. $u_{\text{cell}\backslash\text{SF}}^{2A-i}$ are the displacements at the nodes as represented in Fig. 1. Strains in each SF element (ε^A) and substrate element (ε^M) were evaluated using

$$\varepsilon^{M\backslash A} = \sum_{i=1}^{3} \frac{\partial H_{\text{sub}\backslash\text{SF}i+1}}{\partial x_{\text{sub}\backslash\text{SF}}} u_{\text{sub}\backslash\text{SF}}^{2A-i} \tag{17}$$

Substitution of interpolations in Eq. 16 yields the following discretized equation:

$$\left(\begin{bmatrix} K_{\text{SF}}^A & 0 \\ 0 & K_{\text{sub}}^M \end{bmatrix} + K_c^M \right) \begin{bmatrix} \Delta U_{\text{SF}} \\ \Delta U_{\text{sub}} \end{bmatrix} = R_{\text{assem}}^A \tag{18}$$

K_{SF}^A and K_{sub}^M are the global assembly element stiffness matrices $K_{\text{SF}}^{A\ (e)}$ and $K_{\text{sub}}^{M\ (e)}$ of SF and substrate, respectively

$$K_{\text{SF}}^{A\ (e)} = \int_0^{L^e} \frac{\partial \sigma_{\text{SF}}^A}{\partial X} \left(\frac{\partial H_{\text{SF}}}{\partial x_{\text{SF}}} \right)^T \frac{\partial H_{\text{SF}}}{\partial x_{\text{SF}}} \mathrm{d}L^e \tag{18a}$$

$$K_{\text{sub}}^{M\ (e)} = \int_0^{L^e} E_{\text{sub}} \left(\frac{\partial H_{\text{sub}}}{\partial x_{\text{sub}}} \right)^T \frac{\partial H_{\text{sub}}}{\partial x_{\text{sub}}} \mathrm{d}L^e \tag{18b}$$

K_c^M is the stiffness contribution of n_{eng} clutches engaged between SF elements and substrate elements obtained by global assembly of $K_{c[i]}^M$ represents the contribution of the ith clutch attached at local coordinates $h_{\text{SF}[i]}^A$ and $h_{\text{sub}[i]}^M$. These contributions were assembled into K_c^M, based on indices of SF (A) and substrate (M) elements that represent attachments.

$$K_{c\ [i]}^M = k_c (H_{\text{assem}[i]}{}^T H_{\text{assem}[i]}) \tag{18c}$$

$$H_{\text{assem}[i]} = [H_{\text{SF}}(h_{\text{SF}[i]}^A), -H_{\text{sub}}(h_{\text{sub}[i]}^M)] \tag{18d}$$

R_{assem}^A is the internal residual force of the cell-substrate interaction, which constitutes clutch forces, $F_{\text{assem}[i]}^c$, and the elemental internal force in SF and substrate$F_{\text{int}}^{(e)}$. Both $F_{\text{assem}[i]}^c$ and $F_{\text{int}}^{(e)}$ are assembled into global matrices, F_{assem}^c and F_{int}, based on the associated indices of the element

$$R_{\text{assem}}^A = F_{\text{assem}}^c + F_{\text{int}} \tag{19a}$$

$$F_{\text{int}}^{(e)} = \int_0^{L^e} [H_{\text{SF}} \sigma_{\text{SF}}^A, H_{\text{sub}} \sigma_{\text{sub}}^A]^T \mathrm{d}L^e \tag{19b}$$

$$F_{\text{assem}[i]}^c = (H_{\text{assem}[i]})^T F_{c[i]} \tag{19c}$$

The displacement increments at nodes of the cell and substrate $\Delta U_{\text{sub/SF}}$ were calculated from Eq. 18 using the Newton–Raphson method. Coordinates of the attachment of clutches to the SF, $x_{\text{SF}[i]}$, were updated using Eq. 4.

The SF activation, η, was evaluated at every time step, Δt, to determine the SF contractile stress, σ_{SF}, using Eqs. 6 and 7 in the contractility module. SF contractility results in clutch deformations, $\Delta_{\text{c}[i]}$. SF and substrate displacements,$u_{\text{SF/sub}}$, were updated using deformation increments, $\Delta U_{\text{SF/sub}}$, calculated using Eq. 18. Forces in the clutches, $F_{\text{c}[i]}$, were determined using Eqs. 2 and 5. The clutch deformations were used to determine the engagement/disengagement rates of clutches in the stochasticity module using Eqs. 1 and 3. Deformation $\Delta_{\text{c}[i]}$, clutch forces$F_{\text{c}[i]}$, and membrane deformation, $u_{\text{memb}} = u_{\text{sub}}$, were used as inputs to the calcium signaling module. The population density of high-affinity integrins at the end of engaged clutches, $\xi_{\text{H}[i]}$, was determined from Eq. 8 using $\Delta_{\text{c}[i]}$ and $F_{\text{c}[i]}$. The rate of change in high-affinity integrins was calculated to determine IP_3 production (Eq. 9). The discretized versions of both Eqs. 9 and 11 were integrated using the eighth order Runge–Kutta method to update IP_3 concentration (S) and calcium level (C). Equations 1–11 and 19 were temporally integrated until reaching the simulation time t_{end}. A flowchart for the implementation of the algorithm is shown in Fig S1.

7 Parameters used in the simulation

Table 1 summarizes the simulation parameters for each of the different modules, and the corresponding sources from which these values were obtained. The fibroblast cell length, L_{C}, was assumed to be 60 μm. The reference strain rate $\dot{\varepsilon}_0$ was selected to be 4×10^{-3} so that retrograde velocity of 120 nm/s was obtained at the cell edge. The values of myosin concentration and maximum SF stress (σ_{max}) were selected such that the magnitude of tractions matched experimental data for fibroblasts (Gallant et al. 2005; Balaban et al. 2001). The velocity reduction constant value, $\bar{k}_{\text{v}}$, was selected such that the velocity relation used in Chan and Odde (Chan and Odde 2008) was reproduced in the Hill's equation (Eq. 7). Because most motor-clutch models are limited to results at a single location on the substrate, we used the parameter, k_{sub}, to compare our results with those reported earlier (Chan and Odde 2008). k_{sub} (units = force/length) is the stiffness of the linear spring, which is used to model the local resistance of the underlying substrate. In a previous study, Artola and coworkers used $E_{\text{sub}} = (9 * k_{\text{sub}})/(4\pi a)$, by assuming that the cell exerts uniform traction on the substrate through a circular adhesion site with radius of $a = 0.56$ μm (Elosegui-Artola et al. 2014). The tractions exerted on the substrate, T, were obtained by taking the ratio of local clutch forces with

Table 1 List of variables and values used in the stochastic FE composite model

Parameter	Definition	Value	Source
L_C	Length of the cell [μm]	60	[a]
L_S	Length of the substrate [μm]	120	[a]
η	SF activation	0–1	Deshpande et al. (2006)
k_f	SF formation rate constant [s^{-1}]	120	[a]
k_b	SF dissociation rate constant [s^{-1}]	60	[a]
$\overline{k}_v$	Velocity reduction constant	1	[a]
n_m	Number of myosin motors	8000	[a]
F_m	Motor stall force [pN]	2	Bangasser et al. (2013)
σ_{max}	Maximum stress in SF	$n_m \times F_m$	[a]
σ_0	Isometric stress in SF at activation η	$\eta.\sigma_{max}$	Deshpande et al. (2006)
$\dot{\varepsilon}_0$	Reference SF strain rate [μms^{-1}]	(4×10^{-3})	[a]
n_c	Number of ligands on substrate [μm^{-2}]	420, 740, 1060, 1380	Pathak et al. (2011)
F_b	Integrin-ligand bond rupture force [pN]	8	Deeg et al. (2011)
k_c	Clutch stiffness [nN/μm]	1.5	Deeg et al. (2011)
k_{on}	Clutch on-rate [s^{-1}]	0.1	Roca-Cusachs et al. (2012)
k_{off}^0	Clutch off-rate [s^{-1}]	0.007	Roca-Cusachs et al. (2012)
ξ_R	Reference integrin concentration [μm^{-2}]	3000	Deshpande et al. (2006)
m	Low-affinity integrins mobility [smg^{-1}]	10	Deshpande et al. (2006)
S_0	Reference IP_3 concentration [μm^{-3}]	1000	Pathak et al. (2011)
k_d	de-phosphorylation rate constant of IP_3 [s^{-1}]	5×10^{-4}	Pathak et al. (2011)
m_s	Mobility of IP_3 [smg^{-1}]	10^4	Pathak et al. (2011)
α	Rate of IP_3 production	1	[a]
C	Normalized calcium concentration	0–1	Pathak et al. (2011)
λ_f	Forward rate constant for calcium [s^{-1}]	1	Pathak et al. (2011)
λ_b	Backward rate constant for calcium [s^{-1}]	0.5	Pathak et al. (2011)
k_{sub}	Substrate stiffness [nN/μm]	0.1–1000	[a]

[a]Refers to the present work

focal adhesion area, πa^2, $T = (F_c^{sub}/\pi a^2) \cong F_c^{sub}$. Substrate stiffness, k_{sub}, was chosen in the range 0.1–1000 nN/μm to represent tissue elasticity range observed in vivo. The rate constant for SF formation (k_f) was chosen to be higher than the dissociation constant (k_b) so that SF activation was possible in the absence of stress.

8 Model simulations and parametric analysis

We quantified the effects of ligand density and substrate stiffness on cell–substrate interactions under static and stretch conditions.

Ligand densities corresponding to 420, 740, 1060, and 1380 μm^{-2} were used, and the model was simulated at fifteen different substrate stiffness values ranging between 0.1 and 1000 nN/μm to quantify cellular responses. The static (no-stretch) case was used as control for each of these simulations by imposing zero displacements at the ends of the substrate. These simulations were compared with the cyclic stretch condition of 10% at 1 Hz applied to the substrate. Cell–substrate interactions were evaluated for ~ 10^5 iterations in the stochastic simulations with each condition repeated twenty times. Model outputs include the computed cell tractions at each location of the cell, integrin dynamics, calcium concentrations, and clutch engagements. These were averaged spatially and temporally to explore the combined effects of substrate stiffness and stretch on SF and FA dynamics.

9 Results and discussion

A quantification of cell–substrate interactions under cyclic stretch involves coupling the SF contractility and activation, dynamics of clutch interactions (adaptor proteins) with the substrate, and calcium signaling. We used a novel SFEM framework (Fig. 2; Table 1) to investigate the individual and

combined roles of SF contractility and calcium signaling on clutch engagements/dis-engagements. We also quantified the effects of varied substrate stiffness and cyclic stretch on cell adhesions and tractions. There are three main implications from this study: first, we show that integrin recruitments changed along the cell length. These were low at lamellipodial regions, whereas the highest adhesions were located in lamellar regions. Intracellular calcium resulting from FA dynamics was highest at the lamellipodium. Second, cyclic stretch altered the SF contractility, calcium, and tractions as compared to the static (no-stretch) case. Increased SF contractility was accompanied with a corresponding decrease in integrin recruitments for stretched cells. Finally, cell tractions and adhesions show biphasic responses with substrate stiffness and increased with higher substrate ligand density.

9.1 Effects of SF dynamics and calcium signaling on motor-clutch dynamics

We simulated the effects of calcium signaling and SF contractility on traction generation at FAs for a fibroblast on 10 kPa substrate coated uniformly with 420 μm^{-2} fibronectin density. We explored three different cases to assess the influence of varying SF activation and calcium signaling at the lamellipodia in the model. (i) The motor-clutch model with constant SF activation ($\eta = 1$) and calcium ($C = 1$). This case served as a control to assess the influence of differential SF activation and calcium signaling in the model. (ii) The motor-clutch model with exponentially decaying calcium (time constant, $\theta = 720$ s) illustrates changes in SF remodeling with calcium. (iii) Motor-clutch model with calcium feedback due to integrin clustering caused by the resisting forces of clutches and SF contractile forces.

Figure 3a shows temporal variations in the SF activation due to calcium signaling that leads to changes in the motor-clutch dynamics. SF activation is lower than the control case when the SF is always activated and maintained at a constant value. We quantified the retrograde flow velocity of actin (v), clutch engagements (n_{eng}), and force exerted on substrate for all three cases. Clutches undergo load-fail behaviors and vary cyclically between extrema. These variations are a function of SF contractility and the load-bearing capacity of the clutches (Fig. 3b, c, d). An increase in the force on the ith clutch, ($F_{c[i]}$), results in an increase in the clutch off-rate according to the unloaded off-rate (k_{off} = 0.007 s^{-1}) and characteristic rupture force, F_b (Eq. 1). The retrograde actin flow varied between 10 and 120 nm/s. Tractions in the motor-clutch model varied between 0 and

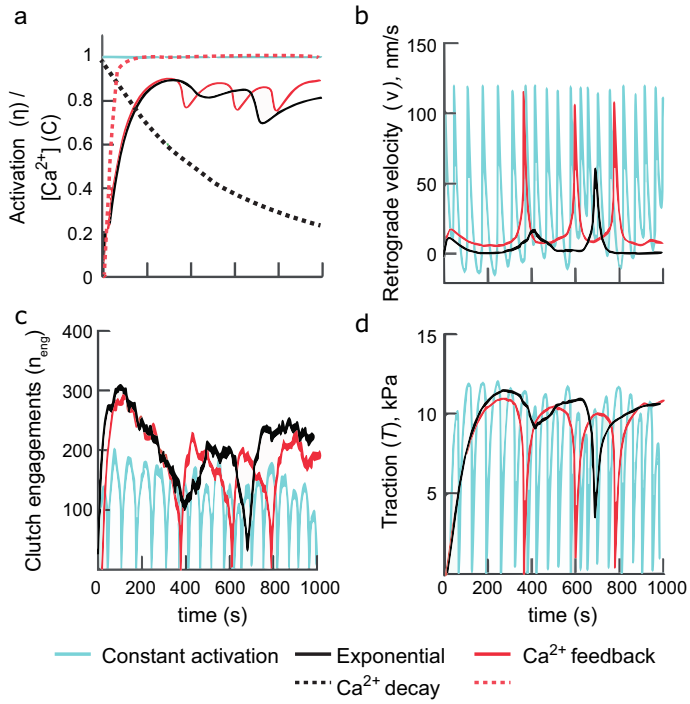

Fig. 3 Motor-clutch dynamics are shown at the lamellipodial (LP) region corresponding to (i) constant activation (η, $C = 1$), (ii) exponential calcium decay, and (iii) calcium feedback due to integrin engagements/clustering and SF remodeling. **a** Temporal evolutions in the SF activation (solid) and calcium are shown for the three different cases (dotted), **b** Retrograde actin flow velocity shows a load-and-fail profile. The variational frequency is dependent on the temporal evolution of SF activation and calcium feedback. **c** Clutch engagements are higher and show lower load-and-fail events with decrease in calcium concentration. **d** Tractions exerted on the substrate bear similarities with the profile for retrograde flow. Maximum tractions were obtained for minimum values of the retrograde flow

12 kPa (Fig. 3b, d). Experiments show a similar range of fibroblast traction with average traction of 3 kPa on a continuous substrate (Humphrey and Rajagopal 2002). The range of forces applied at an adhesion site varied between 0 and 10 nN. Because the SF activation is a constant in the control case (Fig. 3a), the magnitude and frequency variations (~0.018 Hz) in load-and-fail of clutches remain essentially constant. The retrograde actin flow and tractions are inversely related such that the traction maxima corresponds to the minima for retrograde flows. Forces build in the clutches and fail catastrophically (Fig. 3c) when the ensemble reaches load-bearing capacity.

In the second case, SF activation decreased with decaying calcium over time due to decreased calcium (Eq. 6) and cyclical clutch failures (Fig. 3a, c). Retrograde actin flow (v) and tractions (T) reached maximum values of 12.5 nm/s and 11.75 kPa, respectively (Fig. 3b, d). Cyclic variations, clearly identified in the control case, are not as apparent because the SF is not maintained at a maximum value of activation. Decreased SF activation resulted in higher clutch engagements and a corresponding decrease in actin retrograde flow. The velocity does not hence reach the free control velocity value of ~120 nm/s. The model reaches a stalled regime, characterized by near-zero retrograde actin flow, which decreases the cytosolic calcium. The number of engaged clutches was higher with lower retrograde actin flow (Fig. 3a, c).

The influx of calcium from the ER in the third case maintains calcium feedback in the cell (Eqs. 8, 9, and 11). Cyclic variations in clutch engagements resulted in changes to the concentrations of high-affinity integrins (Eq. 9) and were involved with the release of calcium. SF activation, clutch engagements, and the associated tractions varied such that the system did not reach a stalled state (Fig. 3a, c). These simulations show that the calcium signal and SF activity play an important role in the magnitude of cell tractions (Fig. 3d) and retrograde actin flows at the FA regions.

The dynamics of adaptor protein engagements at the FA sites in the motor-clutch model vary with SF contractile force (Chan and Odde 2008). Clutches, represented as slip bonds, reversibly engage with actin. Three separate regimes characterize these interactions: first, *frictional slippage* at low stiffness with an intermediate magnitude of retrograde flow and traction forces. Second, the *load-and-fail* regime at intermediate stiffness with a slow retrograde flow and higher traction forces, and finally, *frictional slippage* at high stiffness with high retrograde flow and low tractions (Bangasser et al. 2013). Lower resistance to actin flow was observed in the frictional slippage region on compliant substrates due to clutch failures before the SF could achieve a maximum possible contractile force. Clutches prematurely fail on compliant substrates as deformations occur at a slower pace than the SF contraction. In contrast, stiff substrates have rapid clutch deformations that result in failures due to lower substrate deformations. The load-and-fail regime was associated with clutches undergoing maximum deformations that collectively fail with SF contraction (Fig. 3c). We see a similar delineation and show that modulations in the cytosolic calcium alters cellular tractions at FAs. These regimes were simulated on a single substrate stiffness with the incorporation of SF remodeling and calcium signaling that has not been discussed in earlier motor-clutch models.

9.2 Spatiotemporal variations in cell–substrate interactions with cyclic stretch

We quantified changes in actin retrograde flow (v), clutch engagements (n_{eng}), traction (T), and calcium signaling at different spatial locations within the adherent cell on a substrate coated with a uniform fibronectin ligand distribution. The substrate had a uniform ligand density, $n_c = 420\ \mu m^{-2}$, and a modulus, $E_{sub}, = 10$ kPa. Simulations were compared for static and cyclic sinusoidal stretch (10% amplitude with 1 Hz frequency) for 10^5 events. The ends of the substrate were initially fixed and then stretched during the subsequent half of the simulation. Figure 4 shows the temporal profile of cell–substrate interactions at the cell interior located ~7.24 μm from the leading edge. Actin retrograde flow velocity and tractions show load-and-fail characteristics under no-stretch conditions with variations between 0 and 60 nm/s and 0–10 kPa at ~5 Hz frequency (Fig. 4a, d). These results are similar to the motor-clutch simulations with calcium feedback and are associated with a change in chemical signaling represented by IP_3 and calcium concentrations (Fig. 4c). Initial clutch engagements cause an accumulation of high-affinity integrins (Fig. 4b), which results in the release of IP_3 and calcium. Excessive deformations cause clutch failures that result in cyclic variations in the clutch forces and corresponding changes in the concentrations of high-affinity integrins (Fig. 4b).

Variations in the rate of IP_3 production due to a changes in the integrin concentrations (Eqs. 9 and 10) resulted in IP_3 concentration changes. Calcium released by IP_3 increased monotonically and plateaued at later time durations. Substrate stretch induces additional forces in clutches that cause perturbations in tractions and high-affinity integrin concentrations. Higher forces in the engaged clutches resulted in higher SF activation and clutch disengagements (Eq. 1) that were accompanied by higher average actin retrograde flow velocity (Fig. 4a). The increase in the integrin density under cyclic stretch caused higher production of IP_3 and a corresponding increase in the cytosolic calcium (Fig. 4b, c). Calcium increase, deformation-induced higher tractions in the cell, and the inverse correlations between traction and

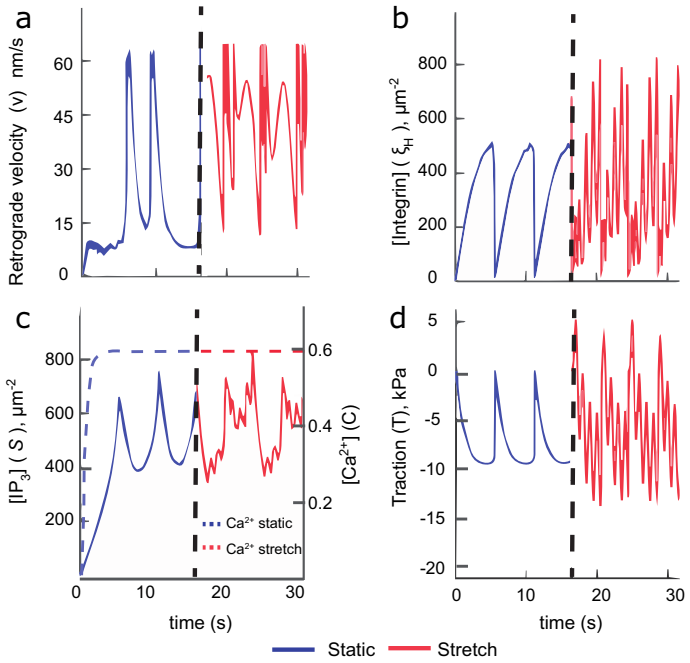

Fig. 4 Temporal evolutions in cell adhesions under static and 10% stretch are shown at node 7 located ~ 7.24 μm from the leading cell edge. 10^5 events were simulated on a 10 kPa substrate with 420 μm^{-2} fibronectin concentration. **a** The retrograde actin velocity for the static case increases with time due to SF activity. Retrograde flows are higher under stretch due to higher SF activation induced by the high-affinity integrin recruitment. **b** The concentration of high-affinity integrins follows load-and-fail behavior with higher variations under stretch. **c** IP_3 production increased with integrin engagement density. Calcium increased with IP_3 concentration and plateaued at a constant level under stretch. **d** Changes in cell tractions resemble the integrin engagement profiles and have maximum values at minimum values of the retrograde velocity

retrograde were also observed under cyclic stretch conditions similar to the control (no-stretch) case. The number of load-and-fail events were however higher under stretch (Fig. 4a, d). Additional clutch deformations under stretch resulted in ~ 50% increase in the traction magnitude and ~ 33.3% increase in high-affinity integrin concentrations.

Figure 5 shows variations in tractions, clutch engagements, high-affinity integrins, and calcium concentrations along the cell length for static and 10% cyclic stretch cases. The asymmetric traction profile about the cell center (node 15) is a consequence of the sign convention employed in the study. Tractions were higher in the transition region adjacent to lamellipodial regions. Lower tractions at the cell center were due to the lower recruitment of high-affinity integrins and greater clutch failures in the lamellipodia. Calcium was higher at the cell center and edges. Tractions, high-affinity integrins, and calcium concentrations have similar profiles under cyclic stretch as the static case but with significantly higher values.

These results show the emergence of three distinct regions in the cell: the lamellipodial (LP) regions in gray, the transition region, and the central region of the cell. A maximum traction of ~ 1.93 kPa was present at nodes 7 and 23 of the cell in the transition region for the static case (Fig. 5a). Lower tractions were observed at the LP regions (1–5 nodes), whereas the cell center had near-zero tractions. The retrograde flow of actin, induced by the contractile strain in the SF, decreased monotonically from the lamellipodial region to the center due to the resistance of clutch engagements. A lower retrograde velocity induces optimum deformation of clutches at lamellar (LA) regions, which resulted in higher tractions (Fig. 5a).

Experiments report decreased actin retrograde flow velocity from the LP to the LA regions of the cell (Plotnikov et al. 2012). Embryonic fibroblasts show an average actin retrograde flow of 11.33 nm/s in the lamellipodial regions and 5.5 nm/s in the lamellar regions. Tractions varied cyclically between ~ 2.5 and 1.89 kPa at the FA. Similar spatial variations in tractions were reported in fibroblasts seeded on polyacrylamide substrates; the maximum traction was 4 kPa at a distance ~ 6 μm from cell edge (Booth-Gauthier et al. 2013). In contrast, fibroblasts on discontinuous pillar-ridge substrate have the highest force (~ 14 nN) at the cell edges (Rathod et al. 2017). Epithelial ptK1 cells also show spatial changes in the actin retrograde velocity and tractions (Gardel et al. 2008). Retrograde velocity monotonically decreased from the cell edge (~ 15 nm/s) to the center (~ 1.5 nm/s). Tractions increased from ~ 25 kPa at the cell edge to ~ 90 kPa

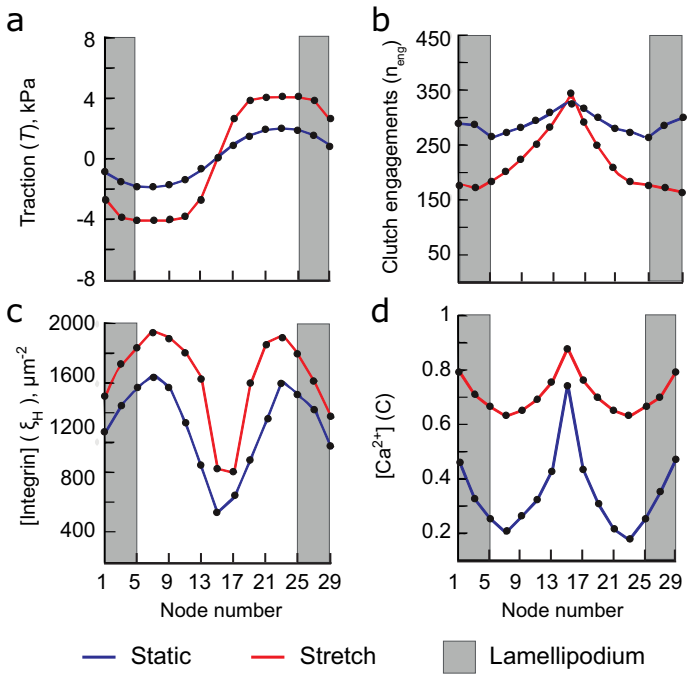

Fig. 5 Spatial variations in **a** tractions, **b** clutch engagements, **c** high-affinity integrin concentration, and **d** calcium concentration over the cell length for static and cyclic stretch conditions

in the intermediate region and were near zero toward the cell center.

Simulations show that tractions under substrate stretch increased by ~ 50% as compared to the static case (Fig. 5a). The overall tractions increased to ~ 4 kPa in the intermediate region and ~ 2.76 kPa at the cell edge. Integrin concentrations increased under cyclic stretch; values were lower in the lamellipodial regions and increased toward the lamellar regions (Fig. 5b). High clutch engagements at the cell center are due to a lower transfer of force through clutches (Fig. 5a). A combination of low tractions and high clutch engagements leads to a stall at the cell center. The lamellipodial and intermediate regions have high tractions and clutch deformations with load-fail profiles (Fig. 4). These results are contrary to those reported earlier by Deshpande and colleagues using a model for SF activation and integrin remodeling (Pathak et al. 2011). Their study showed higher integrin density and tractions at the cell edge that are contrary to data from experiments. These differences may be due to the non-inclusion of slip bond characteristics in the integrin-fibronectin bond that may lead to an increase in the force transfer between cell and substrate at the LP regions. The higher accumulation of high-affinity integrins (ξ_H) at the lamellar and lamellipodium regions correlated with higher traction magnitudes (Fig. 5c). Integrin accumulation at the cell center is primarily driven by a difference in the reference chemical potential between high-affinity and low-affinity integrins. Calcium concentrations show a symmetric profile about the cell center (Fig. 5d) with values higher than the static case. Increased calcium at lamellipodial regions was due to the frequent failure of clutches that caused higher IP_3 at these locations (Fig. 5b); these results agree with experiments on cyclically stretched fibroblasts (Munevar et al. 2004).

9.3 Cellular mechanosensitivity to substrate stiffness

Fibroblasts synthesize and remodel ECM proteins to perform vital functions like tissue maintenance and wound healing (Hinz et al. 2012). We used the model to investigate the role of substrate stiffness and ligand density on cell adhesions under static and cyclic stretch. Figure 6 shows variations in the magnitude of average substrate tractions, clutch engagements, high-affinity integrin, and calcium concentration computed over the entire cell length. We simulated various ligand densities (420, 740, 1060, and 1380 μm^{-2}) and used fifteen distinct substrate stiffness (0.1–1000 nN/μm) to represent a range of in vivo tissue stiffness (Kolahi et al. 2012). The mean clutch forces and high-affinity integrin concentrations were used to compute the average tractions, T_{sub}, and the average integrin concentrations in the study. Data were averaged from 20 simulations at each substrate stiffness and ligand density. Average values with variations are shown in Fig. 6a using error bars.

Cell tractions had a biphasic relationship with the substrate stiffness, k_{sub}. Tractions increased initially with substrate stiffness, reached a maximum value, and subsequently decreased. The presence of additional ligands at high concentrations permit more clutches to bind which increases the load-bearing capability of individual clutches and results in higher tractions (Fig. 6a, b). The (average) high-affinity

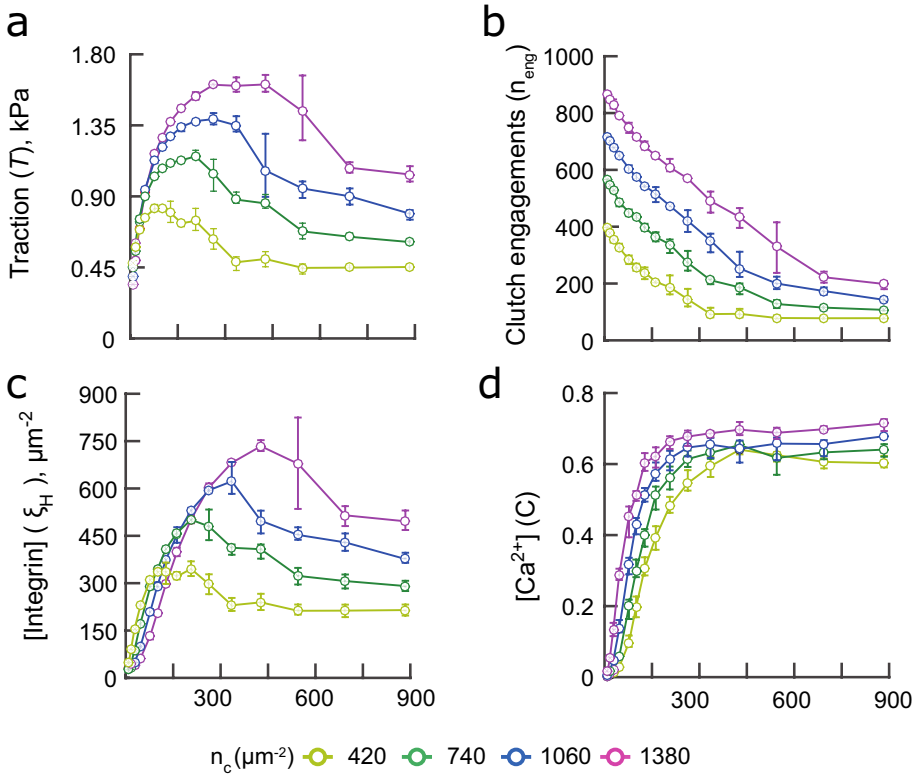

Fig. 6 **a** Cell tractions peak with substrate stiffness under static (no-stretch) condition for each ligand density and plateau to a constant value at higher stiffness for each of the different ligand densities in the study. **b** Clutch engagements, n_{eng}, decreased with substrate stiffness. Higher engagements were visible on substrates coated with greater ligand density. **c** Integrin concentrations, ξ_H, shows a biphasic response with substrate stiffness. **d** Calcium concentrations increased monotonically with substrate stiffness, k_{sub}, and saturated for each ligand density

integrins also display a biphasic relationship with substrate stiffness similar to that of cell tractions (Fig. 6c). An increase in the ligand density on the substrate permits greater integrin accumulations sites and higher integrin recruitments. The associated increase in clutch forces decreases the chemical potential of high-affinity integrins and result in higher tractions (Eq. 9). Substrates with stiffness less than 3 nN/μm, and with low ligand densities, have higher integrin concentrations.

These results put into focus the effects of clutch forces on integrin densities that may outweigh the presence of additional integrin accumulation sites on substrates with low stiffness (Fig. 6c). Higher ligand density and substrate stiffness monotonically enhanced cell spreading and integrin recruitments at FA in fibroblasts (Ghibaudo et al. 2008). Larger FA regions were observed in myoepithelial cells at lower ligand densities on substrates with stiffness < 30 nN/μm; FAs are destabilized on stiffer substrates (Oria et al. 2017). These experiments demonstrate the biphasic nature of integrin recruitments with substrate stiffness. Our results also demonstrate the sensitivity of calcium concentration to substrate properties. Figure 6d shows a rapid increase in calcium at lower substrate stiffness which saturates to a maximum value for each of the different ligand densities in the study. Calcium concentrations remain relatively constant on stiffer substrates. Calcium increases monotonically with an increase in ligand density for a fixed substrate stiffness. Furthermore, the rate of calcium increase is higher on compliant substrates. Our results show that cell mechanosensitivity to substrate stiffness may be tuned by changing the ligand densities on the substrate, which alters calcium signaling.

9.4 Cyclic stretching increases cellular tractions and integrin recruitments at FA

We next investigated cyclic stretch effects on cell tractions, adhesions, and calcium concentrations on substrates with varying ligand densities and stiffness. The (average) substrate tractions, T_{sub}, and high affinity integrin concentrations have a biphasic relationship with substrate stiffness that is similar to no-stretch conditions. These variations have a clearly defined and a relatively sharp peak as compared to the corresponding values for the static case (Fig. 7). Higher ligand densities resulted in increased tractions, clutch engagements, high-affinity integrins, and calcium in cells. Cyclic stretch significantly enhanced tractions on compliant substrates as compared to the static case. In contrast, cyclic stretch resulted in decreasing cell tractions on stiffer substrates. The corresponding values of clutch engagements and high-affinity integrin densities were also significantly lower under cyclic stretch. The maximum cell traction under cyclic stretch ($n_c = 1380\ \mu m^{-2}$) was ~ 50% higher than the corresponding static case; integrin concentrations were also 63% higher under stretch as compared to the static case.

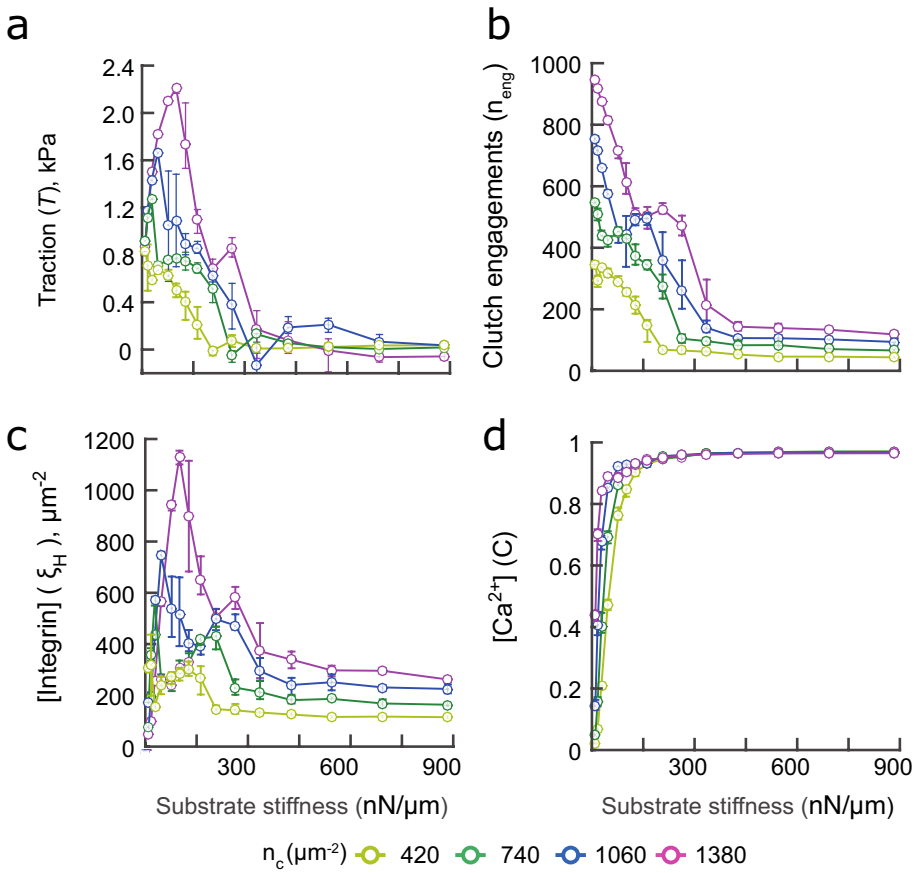

Fig. 7 **a** Variations in the average cell tractions with substrate stiffness under cyclic stretch conditions. Tractions reaches maximum values at an optimal substrate stiffness, k_{sub}^{opt}. **b** Clutch engagements decreased monotonically with substrate stiffness for each of the different ligand densities. **c** Integrin concentrations for engaged clutches, ξ_H, show biphasic response with substrate stiffness. **d** The calcium concentration increased monotonically with substrate stiffness and reached a saturation value for each ligand density. Variation in ligand densities do not have a significant effect on cytosolic calcium. Data were averaged from 20 simulations at each substrate stiffness and ligand density. Average values, along with variations, are shown using error bars in the figure

Clutch engagements decreased with substrate stiffness at a fixed ligand density as seen earlier for cells under no-stretch condition. These values were lower under stretch due to the higher tractions. (Fig. 7b). High ligand density enhances clutch engagements that leads to higher (average) engagement times and forces in clutches. These, in turn, lead to an increase in high-affinity integrins at the cell edge as compared to regions distal to the cell edge where the clutch forces are lower. An increase in ligand density shifts the average integrin recruitments to higher values; integrin concentration in the cell approaches near-zero on substrates with stiffness beyond the critical stiffness (Fig. 7c). Calcium concentrations also increased monotonically with substrate stiffness for all ligand densities similar to the static case and reached a maximum level after ~ 200 nN/μm under cyclic stretch (Fig. 7d). Multiple peaks (Fig. 7a, c) may be due to the non-monotonic clutch engagements under stretch. Actuation of the clutches occur as a consequence of stress fiber contractility, and displacements of substrate ligands under stretch. Because stiffer substrates support forces with less deformation, they are more effective in transferring stretches to clutches. These may result in a plateau in the clutch engagements at intermediate substrate stiffnesses (Fig. 7b).

Experiments demonstrate that fibroblasts subjected to 5% cyclic stretch at 1 Hz frequency have 66% increased tractions (Cui et al. 2015). The underlying difference between the static and cyclic cases may occur due to higher SF activation caused by stretch-aided clutch deformations that result in a higher accumulation of high-affinity integrins and a corresponding elevation in the calcium level (Fig. 7c). Application of 7% stretch on vascular smooth muscle cells increased calcium concentration from ~ 85 nM under no-stretch to ~ 95 nM under cyclic stretch (Lindsey et al. 2008). Model predictions from our study demonstrate that increased tractions are linked to higher SF activity, and coupled to increased calcium and the recruitment of high-affinity integrins at FA in cells under cyclic stretch.

9.5 Optimal substrate stiffness sensing of fibroblasts to cyclic substrate stretch

We quantified substrate stiffness sensing of fibroblasts under cyclic stretch for substrates with varying ligand densities. An optimal substrate stiffness (k_{sub}^{opt}) is defined for the value at which we obtain the maximum (average) traction at a given ligand density. Results were compared between static and cyclic stretch cases for each of the different ligand densities. Simulations from the composite model show that the maximum traction at 420 μm^{-2} ligand density was similar for static and stretch conditions and increased by ~ 40% for 1380

μm^{-2} ligand density (Fig. 8a). The percent increase in average traction due to application of stretch was calculated as

$$\%\ \text{increase in traction} = \frac{\text{average traction under stretch} - \text{average static traction}}{\text{average static traction}} \times 100. \quad (20)$$

Cyclic stretch enhanced tractions for all ligand densities corresponding to compliant substrates in the study; tractions were significantly lower on stiff substrates (Fig. 8b). An increase in the ligand density resulted in higher traction magnitudes over a larger substrate stiffness range. Premature failures of adaptor proteins, connecting the SF and the FA, at low substrate stiffness were prevented under stretch which results in higher tractions. Stretching of substrates with higher stiffness caused clutch overloading which shifts cell–substrate interactions into the frictional-slippage regime and results in lower tractions.

The optimum stiffness shifted toward compliant substrates for all the ligand densities in the study for cells under cyclic stretch (Fig. 8c). The magnitude of shift was greater for higher ligand densities. For example, the optimum substrate stiffness shifted by 90 nN/μm (~95% decrease) at 420 μm^{-2} and by 300 nN/μm (~77.5% decrease) for the 1380 μm^{-2} ligand density. Stretching of substrates stiffer than the critical stiffness significantly reduces fibroblast tractions and integrin recruitments at ligands (Fig. 7a, c). The availability of additional ligands stabilizes adhesions to the substrate and results in an increase in the critical substrate stiffness (Fig. 8d). Near-zero values of tractions also demonstrate cell de-adhesion under stretch at various ligand densities.

Fibroblasts exert contractile stresses on the substrate and continually synthesize/ remodel the underlying substrate (Handorf et al. 2015). Tissue scarring and fibrosis are associated with hyper-production of ECM proteins and a cell transition to myofibroblast phenotype (Herum et al. 2017; Liguo et al. 2016). Myofibroblasts exert high tractions and synthesize ECM proteins to accelerate the tissue remodeling processes (Liguo et al. 2016). High tractions enhance collagen XII production in fibroblasts and trigger reversible phenotypic transition to myofibroblasts (Flück et al. 2003; Kollmannsberger et al. 2018). Cell tractions are also associated with proliferation, chemical signaling, and spreading (Liguo et al. 2016). A quantification of fibroblast tractions under cyclic stretch is hence essential to our understanding of the mechanobiological changes underlying tissue fibrosis.

Figure 9a shows elastic moduli of the tissue under normal and fibrotic conditions that range from low values (< 1 kPa) in soft tissues, such as lungs, to high values (> 500 kPa) in tissues like cartilage (Guimarães et al. 2020). We used

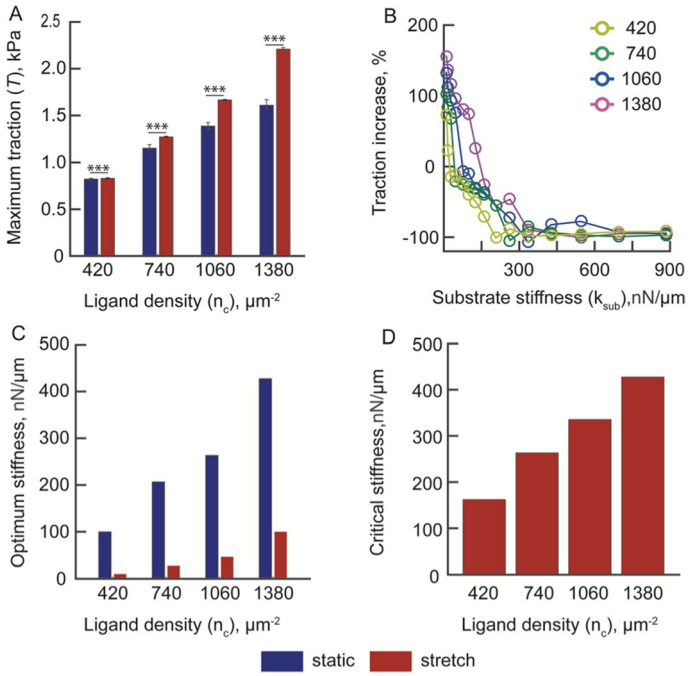

Fig. 8 **a** Maximum traction, *T*, variations as a function of ligand density are shown for 10% cyclic stretch and static conditions. Results between groups were compared using analysis of variance (ANOVA);*** indicates $p < 0.001$. **b** The increase in the traction percent due to stretch as a function of substrate stiffness is plotted for different ligand densities. Substrate stretching increases cell tractions on compliant substrates; the cell tractions however decrease on stiff substrates. **c** Optimum stiffness, computed corresponding to the maximum tractions, are plotted as a function of ligand density. An increase in ligand density shifts the optimum stiffness toward stiffer values in both static and stretch cases. **d** Critical stiffness, characterized by near-zero tractions, increases with ligand density due to stabilization of the adhesions

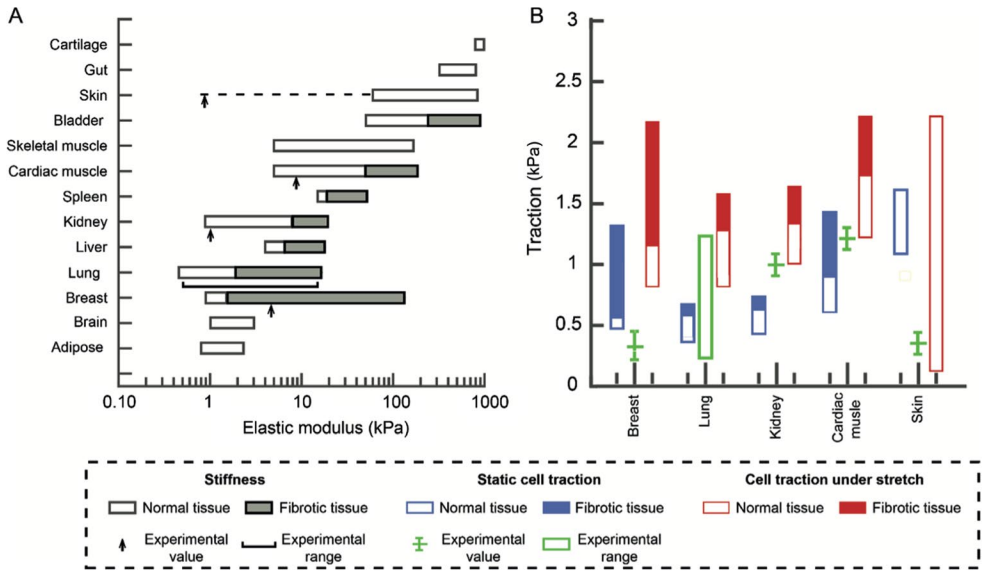

Fig. 9 **a** Stiffness of normal and fibrotic tissues, containing fibroblasts, are shown on a logarithmic scale. Arrows and scale bar indicate substrate stiffness values used in the experiments to compute tractions exerted by fibroblasts. **b** Variations in the average tractions from this study under static and 10% cyclic stretch conditions are shown for fibroblasts in different organs. Green error bars and boxes represent traction values for fibroblasts reported in the literature for fibroblasts. Ligand concentrations corresponding to 1.5 mg/mL collagen I, 10 μg/ml collagen I, 25 μg/ml fibronectin, 50 μg/ml collagen I, and 10 μL collagen I were used for fibroblasts from human breast (Guimarães et al. 2020), lung (Alcoser et al. 2015), kidney (Marinković et al. 2012), cardiac (Tang et al. 2014), and skin (Oh et al. 2018), respectively

our chemomechanical model to compute tractions exerted by fibroblasts on various substrates under static and stretch conditions and compared the simulation results with experiments. Figure 9b shows variations in fibroblast tractions in various organs under static and 10% stretch conditions. Experimental data are included in the figure where available. Model computations show that fibroblast tractions were lower on soft substrates and high on stiffer substrates. Tractions ranged from 0.5 to 1.5 kPa in the static case and 0.2–2.5 kPa for the stretch case that lie in the range of experimentally reported values for fibroblasts in the walls of different organs (Alcoser et al. 2015; Marinković et al. 2012; Tang et al. 2014; Oh et al. 2018; Pauty et al. 2021). Experimentally reported values of mammary fibroblast tractions were lower than the values obtained using our model. Cyclic stretch of 10% caused an overall increase in the computed fibroblast traction magnitudes. Endothelial cells and smooth muscle cells also exhibit mechanosensitivity to the substrate stiffness. Endothelial tractions and adhesions were higher on substrates with higher stiffness and ligand density (Oria et al. 2017). Cyclic stretching enhanced spreading, contractility, and α-SMA expression in endothelial cells (Shao et al. 2014). Smooth muscle cell contractility and spreading increased with stretch on soft substrates (Zeidan et al. 2000). Cyclic stretch resulted in a decrease in the proliferation of smooth muscle cells (Chapman et al. 2000). The feedback between cell tractions and tissue remodeling is hence critical in cell-substrate interactions.

Chan et al. used the motor-clutch model to show an optimal stiffness during cell–substrate interaction at FA (Bangasser et al. 2013). Experiments demonstrate the biphasic relation between average tractions and substrate stiffness for fibroblasts (Marinković et al. 2012). They observed maximum force of 1.5 nN on ~ 15 kPa substrates. Results from our study show a similar biphasic tractions with a maximum value of 1.35 kPa at 1060 μm^{-2}. We considered only one type of integrin ($\alpha_5\beta_1$) in the model and did not include the effects of force loading rate on integrin-fibronectin bond. We have also not included the effects of actin polymerization on adaptor protein assembly. Coupling of chemical signaling with mechanical properties of cell adhesions to substrates clearly demonstrates the effects of SF and FA remodeling under cyclic stretch that has not been shown earlier.

10 Conclusions

We use a systems biology approach to develop a 1D multiscale stochastic finite element model of cellular adhesions to linear elastic substrates of varying stiffness and different ligand densities. The chemo-mechanical model includes focal adhesion attachment dynamics, stress fiber activation, and calcium signaling. We use the model to quantify

tractions along the cell length in response to variations in substrate stiffness, cyclic stretching, and differential ligand densities.

We show that the increase in cytosolic calcium enhances SF formation and results in higher cell tractions and integrin clustering at FA. Mechanical interactions between the SF and reversibly engaging adaptor proteins at FA contribute to the spatiotemporal variations in cell contractility and adhesions reported in experiments. Tractions and adhesion strengths varied along the cell length, and have highest values at intermediate cell regions, and near-zero values in regions proximal to the cell center under static and stretch conditions. Mean tractions and integrin activation in fibroblasts followed biphasic responses with an increase in the substrate stiffness. Cytosolic calcium increased with substrate stiffness and ligand density. The corresponding cell tractions increased with higher ligand density. Cyclic stretch enhances cell tractions and adhesions on compliant substrates. Based on the low tractions obtained from simulations, we show that cells de-adhered from stiff substrates (>50 kPa). Integrin concentrations and tractions reduce to near-zero values beyond the critical substrate stiffness. High substrate stiffness and cyclic stretch increased calcium concentration in cells. Finally, we show that the optimal substrate stiffness at which fibroblasts exert maximum tractions shifted toward compliant substrates with cyclic stretch at a given ligand density.

The model has some limitations: first, a 1D model cannot capture re-orientation dynamics for cells under cyclic stretch reported in the literature (Livne and Geiger 2016; Chatterjee et al. 2022). This will require including an additional spatial dimension to the chemomechanical model. Second, SFs undergo lengthening under uniaxial tension through retrograde actin flows and adaptor protein deformations (Livne and Geiger 2016; Endlich et al. 2007; Chatterjee et al. 2022). We have only explored differences in SF remodeling through integrin reinforcement and have assumed that actin flows induced by contractile SF forces drive clutch deformations. We did not include the growth of the SF under cyclic stretch that is described using exponential growth laws (Chatterjee et al. 2022). We hope to include these aspects in the chemomechanical model in future studies. The findings from our study are novel and contain general principles to explore mechanobiology and cellular contractility.

Supplementary Information The online version contains supplementary material available at https://doi.org/10.1007/s10237-023-01783-6.

Acknowledgements NG gratefully acknowledges the Science and Engineering Research Board, Government of India (SERB/003640 and SERB POWER) for project support.

Author contributions SJ performed the simulations, analyzed the results, and helped write the manuscript. NG designed the study, supervised the research, analyzed results, and wrote the manuscript.

Declarations

Conflict of interest The authors have no conflicts of interest to declare. All co-authors have seen and agree with the contents of the manuscript and there is no financial interest to report. The submission is not under review in any other journal.

References

Alcoser TA, Bordeleau F, Carey SP, Lampi MC, Kowal DR, Somasegar S, Varma S, Shin SJ, Reinhart-King CA (2015) Probing the biophysical properties of primary breast tumor-derived fibroblasts. Cell Mol Bioeng 8:76–85

Arora PD, Bibby KJ, McCulloch CAG (1994) Slow oscillations of free intracellular calcium ion concentration in human fibroblasts responding to mechanical stretch. J Cell Physiol 161(2):187–200

Balaban NQ, Schwarz US, Riveline D, Goichberg P, Tzur G, Sabanay I, Mahalu D, Safran S, Bershadsky A, Addadi L, Geiger B (2001) Force and focal adhesion assembly: a close relationship studied using elastic micropatterned substrates. Nat Cell Biol 3(5):466–472

Bangasser B, Rosenfeld S, Odde D (2013) Determinants of maximal force transmission in a motor-clutch model of cell traction in a compliant microenvironment. Biophys J 105:581–592

Bell GI (1978) Models for the specific adhesion of cells to cells. Science 80(200):618–627

Ben-Ze'ev A, Farmer SR, Penman S (1980) Protein synthesis requires cell-surface contact while nuclear events respond to cell shape in anchorage-dependent fibroblasts. Cell 21:365–372

Besser A, Schwarz US (2007) Coupling biochemistry and mechanics in cell adhesion: a model for inhomogeneous stress fiber contraction. New J Phys 9:425

Booth-Gauthier EA, Du V, Ghibaudo M, Rape AD, Dahl KN, Ladoux B (2013) Hutchinson-Gilford progeria syndrome alters nuclear shape and reduces cell motility in three dimensional model substrates. Integr Biol 5:569–577

Burridge K, Chrzanowska-Wodnicka M (1996) Focal adhesions, contractility, and signaling. Annu Rev Cell Dev Biol 12:463–518

Byron A, Humphries JD, Bass MD, Knight D, Humphries MJ (2011) Proteomic analysis of integrin adhesion complexes. Sci Signal 4:2107–2114

Chagnon-Lessard S, Jean-Ruel H, Godin M, Pelling AE (2017) Cellular orientation is guided by strain gradients. Integr Biol. https://doi.org/10.1039/c7ib00019g

Chan CE, Odde DJ (2008) Traction dynamics of filopodia on compliant substrates. Science 322:1687–1691

Chapman GB, Durante W, Hellums JD, Schafer AI (2000) Physiological cyclic stretch causes cell cycle arrest in cultured vascular smooth muscle cells. Am J Physiol-Heart Circ Physiol 278(3):H748–H754

Chatterjee A, Kondaiah P, Gundiah N (2022) Stress fiber growth and remodeling determines cellular morphomechanics under uniaxial cyclic stretch. Biomech Model Mechanobiol 21(2):553–567. https://doi.org/10.1007/s10237-021-01548-z

Cui Y, Hameed FM, Yang B, Lee K, Pan CQ, Park S, Sheetz M (2015) Cyclic stretching of soft substrates induces spreading and growth. Nat Commun 6:6333

De R (2018) A general model of focal adhesion orientation dynamics in response to static and cyclic stretch. Commun Biol. https://doi.org/10.1038/s42003-018-0084-9

Deeg JA, Louban I, Aydin D, Selhuber-Unkel C, Kessler H, Spatz JP (2011) Impact of local versus global ligand density on cellular adhesion. Nano Lett 11:1469–1476

Deshpande VS, McMeeking RM, Evans AG (2006) A bio-chemo-mechanical model for cell contractility. Proc Natl Acad Sci U S A 103:14015–14020

Elosegui-Artola A, Bazellières E, Allen MD et al (2014) Rigidity sensing and adaptation through regulation of integrin types. Nat Mater 13:631–637

Elson EL, Genin GM (2013) The role of mechanics in actin stress fiber kinetics. Exp Cell Res 319:2490–2500. https://doi.org/10.1016/j.yexcr.2013.06.017

Endlich N, Otey CA, Kriz W, Endlich K (2007) Movement of stress fibers away from focal adhesions identifies focal adhesions as sites of stress fiber assembly in stationary cells. Cell Motil Cytoskelet 64(12):966–976

Flück M, Giraud M-N, Tunç V, Chiquet M (2003) Tensile stress-dependent collagen XII and fibronectin production by fibroblasts requires separate pathways. Biochim Biophys Acta Mol Cell Res 1593:239–248

Galbraith CG, Yamada KM, Sheetz MP (2002) The relationship between force and focal complex development. J Cell Biol 159:695–705

Gallant ND, Michael KE, Garcı J (2005) Cell adhesion strengthening: Contributions of adhesive area, integrin binding, and focal adhesion assembly. Mol Biol Cell 16(9):4329–4340. https://doi.org/10.1091/mbc.E05-02-0170

Gardel ML, Sabass B, Ji L, Danuser G, Schwarz US, Waterman CM (2008) Traction stress in focal adhesions correlates biphasically with actin retrograde flow speed. J Cell Biol 183:999–1005

Ghibaudo M, Saez A, Trichet L, Xayaphoummine A, Browaeys J, Silberzan P, Buguin A, Ladoux B (2008) Traction forces and rigidity sensing regulate cell functions. Soft Matter 4:1836–1843

Grinnell F (1994) Fibroblasts, myofibroblasts, and wound contraction. J Cell Biol 124:401–404

Guimarães CF, Gasperini L, Marques AP, Reis RL (2020) The stiffness of living tissues and its implications for tissue engineering. Nat Rev Mater 5:351–370

Handorf AM, Zhou Y, Halanski MA, Li W-J (2015) Tissue stiffness dictates development, homeostasis, and disease progression. Organogenesis 11:1–15

Herum KM, Choppe J, Kumar A, Engler AJ, McCulloch AD (2017) Mechanical regulation of cardiac fibroblast profibrotic phenotypes. Mol Biol Cell 28:1871–1882

Hinz B, Phan SH, Thannickal VJ, Prunotto M, Desmoulière A, Varga J, De Wever O, Mareel M, Gabbiani G (2012) Recent developments in myofibroblast biology: paradigms for connective tissue remodeling. Am J Pathol 180:1340–1355

Huang C, Miyazaki K, Akaishi S, Watanabe A, Hyakusoku H, Ogawa R (2013) Biological effects of cellular stretch on human dermal fibroblasts. J Plast Reconstr Aesthet Surg 66(12):e351–e361

Humphrey JD, Rajagopal KR (2002) A constrained mixture model for growth and remodeling of soft tissues. Math Model Methods Appl Sci 12(3):407–430

Hynes RO (2002) Integrins: bidirectional, allosteric signaling machines. Cell 110:673–687. https://doi.org/10.1016/S0092-8674(02)00971-6

Janmey PA, Winer JP, Murray ME, Wen Q (2009) The hard life of soft cells. Cell Motil Cytoskelet 66(8):597–605. https://doi.org/10.1002/cm.20382

Kechagia JZ, Ivaska J, Roca-Cusachs P (2019) Integrins as biomechanical sensors of the microenvironment. Nat Rev (mol Cell Biol) 20:457–473. https://doi.org/10.1038/s41580-019-0134-2

Kolahi KS, Donjacour A, Liu X, Lin W, Simbulan RK, Bloise E, Maltepe E, Rinaudo P (2012) Effect of substrate stiffness on early mouse embryo development. PLoS ONE 7:e41717

Kollmannsberger P, Bidan CM, Dunlop JWC, Fratzl P, Vogel V (2018) Tensile forces drive a reversible fibroblast-to-myofibroblast transition during tissue growth in engineered clefts. Sci Adv 4:eaao4881

Kumar A, Ouyang M, Van den Dries K, McGhee EJ, Tanaka K, Anderson MD, Groisman A, Goult BT, Anderson KI, Schwartz MA (2016) Talin tension sensor reveals novel features of focal adhesion force transmission and mechanosensitivity. J Cell Biol 213:371–383

Liguo S, Qu L, Zhu R, Li H, Xue Y, Liu X, Fan J, Fan H (2016) Effects of mechanical stretch on cell proliferation and matrix formation of mesenchymal stem cell and anterior cruciate ligament fibroblast. Stem Cells Int 2016:1–10

Lindsey SH, Tribe RM, Songu-Mize E (2008) Cyclic stretch decreases TRPC4 protein and capacitative calcium entry in rat vascular smooth muscle cells. Life Sci 83:29–34

Livne A, Geiger B (2016) The inner workings of stress fibers—from contractile machinery to focal adhesions and back. J Cell Sci 129:1293–1304. https://doi.org/10.1242/jcs.180927

Livne A, Bouchbinder E, Geiger B (2014) Cell reorientation under cyclic stretching. Nat Commun 106:3938

Lotz MM, Burdsal CA, Erickson HP, McClay DR (1989) Cell adhesion to fibronectin and tenascin: quantitative measurements of initial binding and subsequent strengthening response. J Cell Biol 109:1795–1805

Marinković A, Mih JD, Park J-A, Liu F, Tschumperlin DJ (2012) Improved throughput traction microscopy reveals pivotal role for matrix stiffness in fibroblast contractility and TGF-β responsiveness. Am J Physiol Lung Cell Mol Physiol 303(3):L169–L180. https://doi.org/10.1152/ajplung.00108.2012

Mochitate K, Pawelek P, Grinnell F (1991) Stress relaxation of contracted collagen gels: disruption of actin filament bundles, release of cell surface fibronectin, and down-regulation of DNA and protein synthesis. Exp Cell Res 193:198–207

Muller C, Pompe T (2016) Distinct impacts of substrate elasticity and ligand affinity on traction force evolution. Soft Matter 12:272–280

Munevar S, Wang Y-L, Dembo M (2004) Regulation of mechanical interactions between fibroblasts and the substratum by stretch-activated $Ca2^{+}$ entry. J Cell Sci 117:85–92

Murata N, Ito S, Furuya K, Takahara N, Naruse K, Aso H, Kondo M, Sokabe M, Hasegawa Y (2014) Ca^{+2} influx and ATP release mediated by mechanical stretch in human lung fibroblasts. Biochem Biophys Res Comm 453:101–105

Nishitani WS, Saif TA, Wang Y (2011) Calcium signaling in live cells on elastic gels under mechanical vibration at subcellular levels. PLoS ONE 6(10):e26181

Oh RS, Haak AJ, Smith KMJ, Ligresti G, Choi KM, Xie T, Wang S, Walters PR, Thompson MA, Freeman MR, Manlove LJ, Chu VM, Feghali-Bostwick C, Roden AC, Schymeinsky J, Pabelick CM, Prakash YS, Vassallo R, Tschumperlin DJ (2018) RNAi screening identifies a mechanosensitive ROCK-JAK2-STAT3 network central to myofibroblast activation. J Cell Sci 131:jcs209932

Oria R, Wiegand T, Escribano J, Elosegui-Artola A, Uriarte JJ, Moreno-Pulido C, Platzman I, Delcanale P, Albertazzi L, Navajas D, Trepat X, García-Aznar JM, Cavalcanti-Adam EA, Roca-Cusachs P (2017) Force loading explains spatial sensing of ligands by cells. Nature 552:219–224

Paddillaya N, Ingale K, Gaikwad C, Saini DK, Pullarkat P, Kondaiah GI, Menon, Gundiah N (2022) Cell adhesion strength and tractions are mechano-diagnostic features of cellular invasiveness. Soft Matter 18:4378–4388

Pathak A, Mcmeeking RM, Evans AG, Deshpande VS (2011) An analysis of the cooperative mechano-sensitive feedback between

intracellular signaling, focal adhesion development, and stress fiber contractility. J Appl Mech 78(4):41001–41012
Pauty J, Nakano S, Usuba R, Nakajima T, Johmura Y, Omori S, Sakamoto N, Kikuchi A, Nakanishi M, Matsunaga YT (2021) A 3D tissue model-on-a-chip for studying the effects of human senescent fibroblasts on blood vessels. Biomater Sci 9:199–211
Plotnikov SV, Pasapera AM, Sabass B, Waterman CM (2012) Force fluctuations within focal adhesions mediate ECM-rigidity sensing to guide directed cell migration. Cell 151:1513–1527
Rathod ML, Pareek N, Agrawal S, Jaddivada S, Lee DW, Gundiah N (2017) Engineered ridge and micropillar array detectors to quantify the directional migration of fibroblasts. RSC Adv 7:51436–51443
Roca-Cusachs P, Iskratsch T, Sheetz MP (2012) Finding the weakest link: exploring integrin-mediated mechanical molecular pathways. J Cell Sci 125:3025–3038
Shao Y, Mann JM, Chen W, Fu J (2014) Global architecture of the F-actin cytoskeleton regulates cell shape-dependent endothelial mechanotransduction. Integr Biol 6:300–311
Swaminathan V, Kalappurakkal JM, Mehta SB, Nordenfelt P, Moore TI, Koga N, Baker DA, Oldenbourg R, Tani T, Mayor S, Springer TA, Waterman CM (2017) Actin retrograde flow actively aligns and orients ligand-engaged integrins in focal adhesions. Proc Natl Acad Sci 114:10648
Takagi J, Petre BM, Walz T, Springer TA (2002) Global conformational rearrangements in integrin extracellular domains in outside-in and inside-out signaling. Cell 110:599–611
Takagi J, Strokovich K, Springer TA, Walz T (2003) Structure of integrin alpha5beta1 in complex with fibronectin. EMBO J 22:4607–4615
Tang X, Tofangchi A, Anand SV, Saif TA (2014) A novel cell traction force microscopy to study multi-cellular system. PLoS Comput Biol 10:e1003631
Tiwari S, Askari JA, Humphries MJ, Bulleid NJ (2011) Divalent cations regulate the folding and activation status of integrins during their intracellular trafficking. J Cell Sci 124:1672–1680
Wang JHC, Yang G, Li Z, Shen W (2004) Fibroblast responses to cyclic mechanical stretching depend on cell orientation to the stretching direction. J Biomech 37(4):573–576
Ward MD, Hammer DA (1993) A theoretical analysis for the effect of focal contact formation on cell-substrate attachment strength. Biophys J 64(3):936–959
Watt FM, Jordan PW, O'Neill CH (1988) Cell shape controls terminal differentiation of human epidermal keratinocytes. Proc Natl Acad Sci USA 85:5576–5580
Winograd-Katz SE, Fassler R, Geiger B, Legate KR (2014) The integrin adhesome: from genes and proteins to human disease. Nat Rev Mol Cell Biol 15:273–288
Wozniak MA, Modzelewska K, Kwong L, Keely PJ (2004) Focal adhesion regulation of cell behavior. Biochim Biophys Acta 1692:103–119
Zeidan A, Nordström I, Dreja K, Malmqvist U, Hellstrand P (2000) Stretch-dependent modulation of contractility and growth in smooth muscle of rat portal vein. Circ Res 87:228–234